Dendrite-targeting OLM interneurons regulate the formation of learning-related CA1 place cell representations.

Evan P. Campbell[1*], Lisandro Martin[2*], Jeffrey C. Magee[1#], Christine Grienberger[2#]

[1]Howard Hughes Medical Institute, Baylor College of Medicine, Houston, TX, 77030

[2]Brandeis University, Department of Biology and Volen Center for Complex Systems, Waltham, MA, 02453

* Equal contribution

Co-last authors

Correspondence to: Christine Grienberger
Brandeis University
Department of Biology
415 South Street, Waltham, MA, 02453, USA
Email: cgrienberger@brandeis.edu

Spatial learning depends on the rapid formation of hippocampal CA1 place cell representations through behavioral timescale synaptic plasticity (BTSP)[1-7]. BTSP is driven by dendritic Ca^{2+} plateau potentials in the distal apical dendrites of CA1 pyramidal neurons and is thought to arise from the interaction of an excitatory target signal from entorhinal cortex layer 3 (EC3) with inhibitory feedback reflecting the current CA1 population state[8]. However, the cellular source of this feedback remains unknown. To identify this circuit element, we combined in vivo two-photon calcium imaging with bidirectional optogenetic manipulation to examine the role of dendrite-targeting oriens lacunosum-moleculare (OLM) interneurons[9,10]. We found that axonal and somatic activity of OLM interneurons increased with learning and was spatially biased toward behaviorally salient locations, closely matching the evolving CA1 population representation and the environment-specific EC3 target signal[3]. Causal manipulations revealed that optogenetic silencing of Chrna2α-positive OLM interneurons, a genetically defined OLM subset, late in learning increased dendritic plateaus and promoted place cell formation at stimulated locations, whereas activation of the same population early in learning suppressed plateau initiation and place field formation. Together, these findings identify OLM interneurons as the key inhibitory feedback element that dynamically regulates BTSP and stabilizes hippocampal representations during learning.

OLM axonal activity increases with spatial learning.

Spatial learning engages behavioral timescale synaptic plasticity (BTSP), which is triggered by Ca^{2+} plateau potentials ("plateaus") in the distal apical tuft dendrites of CA1 pyramidal neurons[11-13] and generates CA1 place cell representations[1-7]. In previous work, we showed that entorhinal cortex layer 3 (EC3) provides a stable, target-like excitatory input enhanced at behaviorally salient locations, which promotes dendritic plateau initiation and drives BTSP, shaping CA1 population activity toward an overrepresentation of salient locations required for successful spatial learning[14-18]. We hypothesize that plateau initiation reflects a mismatch between the EC3-derived excitatory target signal and an inhibitory feedback signal that reports the current state of the CA1 population, leading to plateau activity when excitatory drive exceeds feedback inhibition (Fig. 1a). *Oriens–lacunosum moleculare* (OLM) interneurons are well positioned to provide such feedback, as they

53 receive excitatory input from CA1 pyramidal neurons and selectively target the tuft dendritic
54 compartment[19-21].

55 To test whether OLM interneurons constitute the inhibitory feedback signal, we performed
56 two-photon Ca^{2+} imaging of OLM axons in dorsal CA1 of somatostatin (SST)-IRES-Cre mice[22]
57 expressing the Ca^{2+} indicator GCaMP6f and tdTomato while animals ran on a linear treadmill
58 (with three somatosensory cues) and learned a fixed reward location (Fig. 1b). OLM axonal Ca^{2+}
59 signals were recorded in *stratum lacunosum-moleculare* (SLM), the CA1 sublayer where
60 entorhinal cortex layer 3 (EC3) inputs converge with OLM-mediated inhibition and averaged
61 within each field of view to yield a population-level measure of OLM output alongside behavioral
62 variables (Fig. 1c, Extended Data Fig. 1a). As in prior work[3,14], animals restricted their licking to
63 the region surrounding the reward and reduced their running speed when approaching the reward
64 delivery site during the day 1 session (belt with tactile cues, fixed reward) when comparing early
65 (quintile 1) to later laps (quintile 5; Fig. 1d). These behavioral changes were not observed during
66 the day 0 sessions (last day of habituation; no cues, random reward), when licking and running
67 speed remained relatively uniform across space. On day 1 and subsequent recording sessions, after
68 correcting for dwell time to account for learning-related changes in running speed, OLM axonal
69 Ca^{2+} activity developed spatial structure, increasing modestly across the track but exhibiting a
70 pronounced peak at the reward location during later laps (Fig. 1e–i, Extended Data Fig. 1b–g). A
71 comparable learning-dependent increase in OLM activity at salient locations was observed in a
72 separate group of animals recorded in a distinct environment, in which animals ran on a blank belt
73 and a visual cue was positioned 50 cm before the reward (Extended Data Fig. 2). In this
74 environment, OLM axonal activity likewise increased with learning but instead peaked near the
75 cue location.

76 Because our prior work has shown that both EC3 target patterns and CA1 representations
77 differ across these two environments[3], the corresponding shifts in OLM activity we observe here
78 indicate that these interneurons track the evolving CA1 population state and align with the
79 environment-specific EC3 target structure. Together, our results identify OLM interneurons as the
80 likely source of a learning-dependent inhibitory feedback signal that interacts with the entorhinal
81 excitatory input at distal apical dendrites to regulate plateau initiation during learning. Notably,
82 we observed the OLM activity development despite averaging across all axons within the imaging

83 plane, potentially suggesting a population-level modulation of OLM output rather than the
84 emergence of highly selective individual axons.
85
86 **Spatial learning induces population-wide changes in OLM interneuron activity.**
87 Therefore, to determine whether the learning-related OLM activity change observed at the
88 population axonal level reflected coordinated, experience-dependent changes in a large population
89 of OLM interneurons rather than being driven by a small subset of strongly modulated cells, we
90 examined Ca^{2+} dynamics in the somata of identified OLM interneurons during the same behavioral
91 paradigm. For these experiments, we used a Chrna2α-Cre mouse line, which provides selective
92 and reliable genetic access to OLM interneurons[20,23], and performed two-photon Ca^{2+} imaging of
93 OLM somata located in *stratum oriens*, where OLM cell bodies reside (Fig. 2a). Two-photon
94 imaging revealed sparsely labeled Chrna2α-positive OLM somata within each field of view,
95 allowing for the analysis of single-cell neuron activity. Example traces from three OLM neurons
96 illustrate heterogeneous but coordinated activity across laps (Fig. 2b). We first quantified the
97 population-averaged OLM somatic activity (Fig. 2c-g) and found that it closely matched the spatial
98 and temporal profiles observed for SST axonal activity (Fig. 1, Extended Data Fig. 1b-g),
99 indicating that the axonal signal reflects changes in OLM activity rather than additional axonal
100 processing. Next, we examined how learning shaped activity patterns at the individual neuron level
101 (Fig. 2h-n). Spatially binned, dwell-time–corrected activity maps from three example neurons
102 illustrate an increase in activity primarily at the reward location over the course of the session in
103 all three cells (Fig. 2h). Consistent with this, heatmaps summarizing the activity of all recorded
104 Chrna2α-positive OLM neurons (n = 57) during early (quintile 1) and late (quintile 5) phases of
105 the session reveal a population-wide increase in activity at the reward location (Fig. 2i). Consistent
106 with this observation, quantitative analyses showed modest but significant increases in both spatial
107 and reward selectivity in quintile 5 compared to quintile 1 across the OLM population (Fig. 2j–l).
108 In addition, the peak activity location of individual neurons shifted toward the reward location
109 over the course of the session (on average 13.3 +/- 3.1 cm), with a wide distribution of shift
110 magnitudes but with 73.7% of the population shifting closer to reward (Fig. 2m). Notably, neurons
111 whose activity peaks were initially located farther from the reward exhibited larger shifts by the
112 end of learning (Fig. 2n). Together, these results demonstrate that learning-related changes in OLM

activity are distributed across the population, with most neurons contributing to the evolving increase in inhibitory feedback signal to varying degrees.

Silencing OLM interneurons late in learning permits BTSP-mediated place cell formation. If OLM activity indeed constitutes the inhibitory feedback predicted to regulate BTSP, then manipulating OLM activity should bidirectionally constrain plateau initiation and place field formation. To test this hypothesis, we first optogenetically suppressed Chrna2α-positive OLM interneurons during spatial learning using a combined transgenic and viral strategy that enabled simultaneous Ca^{2+} imaging and optogenetic manipulation, with GCaMP6f expressed in CA1 pyramidal neurons and ArchT selectively expressed in OLM interneurons (Fig. 3a-b). Optogenetic manipulation was restricted to an "opto-zone" centered around the fixed reward location (Fig. 3a). Each session was divided into two blocks, with no light delivered during block 1 (laps 1–50) and OLM silencing during block 2 (laps 51–100) via 594 nm-light activation of archaerhodopsin-T (ArchT)[24] (Fig. 3a). This design allowed us to perturb OLM activity late in learning around the reward, when and where OLM activity is highest (Figs. 1–2). Mice that did not express ArchT but were otherwise treated identically served as controls; in a subset of animals, we further confirmed that 594 nm-light effectively suppressed the activity of ArchT-expressing Chrna2α-positive interneurons (Extended Data Fig. 3a–f). Importantly, this optogenetic manipulation did not alter running or licking behavior, indicating that ArchT activation did not disrupt task engagement or reward anticipation (Fig. 3c). Consistent with the absence of optogenetic manipulation during block 1, CA1 place cell activity was similar in control and ArchT-expressing animals during this initial phase of the session (Fig. 3d–e, Extended Data Fig. 4a–c). In contrast, during block 2, silencing OLM neurons resulted in an increase in place cell density within the opto-zone around the reward in ArchT-expressing animals (Fig. 3d–e). To quantify the temporal dynamics of this effect, we analyzed the emergence of new place fields, distinguishing fields whose peaks fell within the opto-zone from those located in an "away-zone" approximately 90 cm from the opto-zone (Fig. 3f). In ArchT-expressing animals, new place field formation increased selectively within the opto-zone during block 2, with no corresponding change in the away-zone. As a consequence, the fraction of CA1 place cells was significantly higher in the opto-zone during block 2 in ArchT-expressing animals compared to controls, while no differences were observed in block

143 1 or outside the opto-zone (Fig. 3g). Together, these data indicate that OLM suppression
144 selectively facilitates place cell formation at the manipulated location and late stage of learning.
145 To determine whether this increase in place field formation in the block 2 opto-zone was
146 associated with an increase in plateau activity, we next identified putative dendritic plateaus using
147 established Ca^{2+} imaging signatures with GCaMP6f, derived from prior whole-cell and imaging
148 studies[1,3,25,26]. Plateau events were defined as a large-amplitude Ca^{2+} transient followed by
149 sustained increases in activity across at least three subsequent laps relative to pre-event activity
150 levels, with only the first qualifying event per cell included in the analysis[1,3,25,26] (Fig. 3h–k,
151 Extended Data Fig. 5a-b, see Method section). We found that the CA1 population in control
152 animals exhibited a marked reduction in plateau probability from block 1 to block 2 (Fig. 3j–k;
153 46% (± 4) of CA1 neurons exhibited a plateau in block 1 vs. 10% ± 0.8 in block 2, Full belt, mean
154 ±SEM paired two-tailed *t*-test, $P<1\bullet10^{-4}$), with plateaus preferentially concentrated near the reward
155 location. A similar global reduction in plateau probability was observed in ArchT-expressing
156 animals (51% ± 4 vs. 17% ± 1, block 1 vs. block 2 full belt; paired two-tailed t-test, $P<1\bullet10^{-4}$).
157 However, compared with controls, the probability of observing a plateau event during later laps in
158 block 2 was significantly elevated in ArchT animals (unpaired two-tailed t-test, $P<1\bullet10^{-4}$). This
159 effect was driven by an approximately 2.5-fold increase in plateau probability within the center of
160 the opto-zone relative to controls (Fig. 3j–k), indicating a selective enhancement of plateau activity
161 at the manipulated location. Notably, the amplitudes of the lower 80% of Ca^{2+} events (used as a
162 proxy for non-plateau-related neuronal activity) measured in the opto-zone were not significantly
163 affected by ArchT activation (Extended Data Fig. 5c).
164 Together, these results indicate that OLM interneuron activity constrains BTSP-mediated
165 place cell formation by suppressing dendritic plateau initiation in CA1 pyramidal neurons.
166 Silencing OLM neurons during the later phase of learning selectively releases this constraint,
167 allowing additional place fields to form at the reward location, driven by the excitatory input
168 pattern from EC3.
169
170 **Activating OLM interneurons early in learning suppresses BTSP-mediated place cell**
171 **formation.**
172 To test whether OLM interneuron activity is sufficient to suppress place cell formation, we next
173 performed optogenetic activation of Chrna2α-positive OLM neurons during the early phase of

174 spatial learning (Fig. 4, Extended Data Fig. 3g-l). OLM neurons expressing ReaChR[27]
175 (Chrna2α:ReaChR mice) were selectively activated within the opto-zone during block 1, a phase
176 when place cell formation and BTSP induction are generally high due to low OLM activity (Figs.
177 1–2). CA1 pyramidal neurons were imaged following AAV-mediated expression of GCaMP6f in
178 Chrna2α:ReaChR mice. Activation of OLM interneurons during block 1 significantly inhibited
179 the development of CA1 spatial representations (Fig. 4a–e; Extended Data Fig. 4d-f). Heatmaps
180 of CA1 population activity revealed a marked reduction in the emergence of place fields within
181 the opto-zone surrounding the reward in ReaChR-expressing animals compared to controls. This
182 suppression was evident both in the overall number of place cells and in their spatial distribution
183 (Fig. 4a-e), indicating that increased OLM-mediated inhibition during early learning constrains the
184 formation of new place fields. Consistent with the block-specific manipulation, place cell
185 development during block 2 was comparable between groups once the optogenetic manipulation
186 was discontinued. These results demonstrate that increasing OLM activity is sufficient to suppress
187 place cell formation during early learning when the probability of BTSP induction is high.
188 We next asked whether this suppression was due to altered plateau probability. Using the
189 same Ca^{2+} imaging-based criteria as before (Fig. 3h), we identified putative dendritic plateau
190 events (Fig. 4f–g, Extended Data Fig. 5d–e, see Method section). In ReaChR-expressing animals,
191 plateau events were significantly reduced during block 1 in the opto-zone (Fig. 4f), consistent with
192 OLM activation suppressing plateau initiation in CA1 pyramidal neurons. We further found that,
193 while control animals showed an approximate 2-fold increase in plateau probability at the reward,
194 this enrichment was lost in ReaChR animals (1.90±0.09 fold vs. 1.07±0.33 fold for controls vs.
195 ReaChR animals, bin 5/mean of bins 1–3, unpaired two-tailed *t*-test $P=2.97 \cdot 10^{-2}$). Following the
196 end of OLM activation, plateau occurrence returned to control levels, paralleling the normalization
197 of place field formation. Importantly, this effect was not accompanied by a global change in
198 neuronal activity, as the amplitudes of the lower 80% of Ca^{2+} events were not significantly altered
199 by ReaChR activation (Extended Data Fig. 5f). Together, these experiments demonstrate that
200 increasing OLM interneuron activity early in learning is sufficient to suppress BTSP-mediated
201 place field formation.
202
203
204

Summary and Conclusions

Here, we address a central question left open by our prior work establishing BTSP as a mechanism for experience-dependent hippocampal learning: why BTSP-mediated place field formation declines with learning despite a stable EC3 target signal. We identify a learning-dependent, circuit-level inhibitory feedback signal that dynamically regulates when and where BTSP can occur (Fig. 4h–i). OLM interneurons provide this feedback, consistent with their known circuit position as recipients of excitatory input from CA1 pyramidal neurons and inhibitors of distal apical tuft dendrites. Early in learning, low OLM activity permits EC3-driven excitation to trigger dendritic plateaus and robust BTSP-mediated place field formation; as learning proceeds and CA1 population activity increases, recruitment of OLM-mediated inhibition progressively suppresses further plateau initiation. Rather than simply suppressing plasticity, this feedback enables the development of hippocampal representations to terminate once they have converged on their target pattern. This model is supported by our optogenetic manipulations: activating OLM interneurons early suppresses plateau initiation and place field formation, whereas silencing them later reinstates plateau firing and BTSP and enables additional place fields to emerge. Together, these findings establish OLM interneurons as a core control element that stabilizes hippocampal representations by constraining plasticity once learning has occurred, while preserving the capacity for rapid adaptation when representations remain incomplete or inaccurate.

Our results provide additional experimental support for the idea that dendritic plateaus act as locally computed error signals. Rather than requiring the explicit broadcasting of a global error across the circuit[28], plateau initiation in individual CA1 neurons depends on whether excitation exceeds inhibition within their tuft compartment, providing a cell-specific signal that additional synaptic modification is warranted. This computation may be well-suited for guiding learning in complex neuronal networks because it implicitly accounts for the many parameters that link activity across brain circuits to behavior[28-30]. OLM interneurons are uniquely positioned to implement this form of inhibitory feedback, and our data indicate that learning-dependent changes in their activity are distributed across the population, consistent with them broadly sampling the evolving CA1 representation. Consistent with this interpretation, OLM activity on subsequent training days developed the reward peak more rapidly than on day 1 (Extended Data Fig. 1f-g), reflecting the accelerated stabilization of experience-dependent CA1 representations of salient locations[25]. An additional feature of this mechanism is its generality across behavioral contexts.

We found OLM axonal activity was biased toward behaviorally salient locations across environments with distinct EC3 target patterns, including one in which salience was defined by a visual cue rather than by reward delivery. Thus, OLM-mediated feedback appears not to be tied to reward per se but rather to reflect task-relevant structure. Such flexibility may be essential for spatial learning in natural environments, where the nature of salient features varies across contexts and over time.

Our results identify OLM interneurons (and specifically the Chrna2α-positive subtype) as a central control element of BTSP. However, a growing body of work suggests that additional interneuron classes play an important role in regulating hippocampal plasticity. Interneurons targeting the soma and distinct dendritic compartments exhibit task-related activity changes during goal-directed learning, interact bidirectionally with OLM cells in a state- and context-dependent manner, and influence place field activity when manipulated[9,20,23,31-37]. In hippocampal slices, dendrite-targeting interneurons control dendritic plateau initiation[38,39], and recent work has shown that a distinct OLM subtype (i.e., NDNF/Nkx2-1-expressing) regulates plateau termination *in vitro*[40]. Disinhibitory circuits involving VIP interneurons provide an additional layer of control. VIP interneurons, which are activated by novelty[41], influence the development of hippocampal spatial representations and are thought to act indirectly through OLM-mediated disinhibition of distal apical dendrites[14,42]. This mechanism has recently been linked to BTSP[42]. Beyond local inhibitory circuits, neuromodulatory systems are also likely to shape BTSP-mediated place cell formation[43], hippocampal plasticity[44], and, more broadly, the balance between dendritic excitation and inhibition during learning[45]. For example, cholinergic subcortical nuclei directly innervate hippocampal OLM interneurons, while VIP interneurons also receive neuromodulatory input, suggesting that neuromodulation may scale OLM activity at multiple circuit levels during reward-based learning[46]. Future work will be required to determine how these inhibitory and neuromodulatory pathways interact, either through OLM interneurons or in parallel, to regulate BTSP during behavior.

Together, our findings demonstrate that learning in hippocampal circuits is governed by a dendritic feedback computation that provides a biologically grounded mechanism for controlling synaptic plasticity at behavioral timescales and across hierarchically organized circuits and may generalize to other brain regions that require balancing flexibility with stability.

Acknowledgements

We thank Randy Chitwood and Francisco Mello for technical assistance. We thank Andreas Tolias, Klas Kullander, Simon Chamberland, Richard Tsien, Jun Wu, and Gina Poe for generously providing the SST-IRES-Cre and Chrna2α-Cre mouse lines. We also thank Randy Chitwood, Aaron Milstein, and Sachin Vaidya for valuable discussions. This work was supported by the NIH 4RF1 MH135576 (CG), 1DP2 MH136393 (CG), the Howard Hughes Medical Institute (JCM), and the Cullen Foundation (JCM).

Author Contributions

EPC, LM, JCM, and CG designed the research. EPC, LM, and CG performed *in vivo* recordings. EPC, LM, JCM, and CG analyzed the data and wrote the manuscript.

Competing Financial Interests

The authors declare no competing financial interests.

References

1 Bittner, K. C., Milstein, A. D., Grienberger, C., Romani, S. & Magee, J. C. Behavioral time scale synaptic plasticity underlies CA1 place fields. *Science* **357**, 1033-1036, doi:10.1126/science.aan3846 (2017).

2 Fan, L. Z. *et al.* All-optical physiology resolves a synaptic basis for behavioral timescale plasticity. *Cell* **186**, 543-559 e519, doi:10.1016/j.cell.2022.12.035 (2023).

3 Grienberger, C. & Magee, J. C. Entorhinal cortex directs learning-related changes in CA1 representations. *Nature* **611**, 554-562, doi:10.1038/s41586-022-05378-6 (2022).

4 Milstein, A. D. *et al.* Bidirectional synaptic plasticity rapidly modifies hippocampal representations. *Elife* **10**, doi:10.7554/eLife.73046 (2021).

5 Gonzalez, K. C. *et al.* Synaptic basis of feature selectivity in hippocampal neurons. *Nature* **637**, 1152-1160, doi:10.1038/s41586-024-08325-9 (2025).

6 Diamantaki, M. *et al.* Manipulating Hippocampal Place Cell Activity by Single-Cell Stimulation in Freely Moving Mice. *Cell Rep* **23**, 32-38, doi:10.1016/j.celrep.2018.03.031 (2018).

7 Zhao, X., Hsu, C. L. & Spruston, N. Rapid synaptic plasticity contributes to a learned conjunctive code of position and choice-related information in the hippocampus. *Neuron* **110**, 96-108 e104, doi:10.1016/j.neuron.2021.10.003 (2022).

8 Magee, J. C. & Grienberger, C. Synaptic Plasticity Forms and Functions. *Annu Rev Neurosci* **43**, 95-117, doi:10.1146/annurev-neuro-090919-022842 (2020).

9 Udakis, M., Claydon, M. D. B., Zhu, H. W., Oakes, E. C. & Mellor, J. R. Hippocampal OLM interneurons regulate CA1 place cell plasticity and remapping. *Nat Commun* **16**, 9912, doi:10.1038/s41467-025-64859-0 (2025).

10 Royer, S. *et al.* Control of timing, rate and bursts of hippocampal place cells by dendritic and somatic inhibition. *Nat Neurosci* **15**, 769-775, doi:10.1038/nn.3077 (2012).

11 Grienberger, C., Chen, X. & Konnerth, A. NMDA receptor-dependent multidendrite Ca(2+) spikes required for hippocampal burst firing in vivo. *Neuron* **81**, 1274-1281, doi:10.1016/j.neuron.2014.01.014 (2014).

12 Takahashi, H. & Magee, J. C. Pathway interactions and synaptic plasticity in the dendritic tuft regions of CA1 pyramidal neurons. *Neuron* **62**, 102-111, doi:10.1016/j.neuron.2009.03.007 (2009).

13 O'Hare, J. K., Wang, J., Shala, M. D., Polleux, F. & Losonczy, A. Distal tuft dendrites predict properties of new hippocampal place fields. *Neuron* **113**, 1969-1982 e1967, doi:10.1016/j.neuron.2025.03.029 (2025).

14 Turi, G. F. *et al.* Vasoactive Intestinal Polypeptide-Expressing Interneurons in the Hippocampus Support Goal-Oriented Spatial Learning. *Neuron* **101**, 1150-1165 e1158, doi:10.1016/j.neuron.2019.01.009 (2019).

15 Zaremba, J. D. *et al.* Impaired hippocampal place cell dynamics in a mouse model of the 22q11.2 deletion. *Nat Neurosci* **20**, 1612-1623, doi:10.1038/nn.4634 (2017).

16 Dupret, D., O'Neill, J., Pleydell-Bouverie, B. & Csicsvari, J. The reorganization and reactivation of hippocampal maps predict spatial memory performance. *Nat Neurosci* **13**, 995-1002, doi:10.1038/nn.2599 (2010).

17 Hollup, S. A., Molden, S., Donnett, J. G., Moser, M. B. & Moser, E. I. Accumulation of hippocampal place fields at the goal location in an annular watermaze task. *J Neurosci* **21**, 1635-1644, doi:10.1523/JNEUROSCI.21-05-01635.2001 (2001).

18 Gauthier, J. L. & Tank, D. W. A Dedicated Population for Reward Coding in the Hippocampus. *Neuron* **99**, 179-193 e177, doi:10.1016/j.neuron.2018.06.008 (2018).

19 Klausberger, T. GABAergic interneurons targeting dendrites of pyramidal cells in the CA1 area of the hippocampus. *Eur J Neurosci* **30**, 947-957, doi:10.1111/j.1460-9568.2009.06913.x (2009).

20 Chamberland, S. *et al.* Functional specialization of hippocampal somatostatin-expressing interneurons. *Proc Natl Acad Sci U S A* **121**, e2306382121, doi:10.1073/pnas.2306382121 (2024).

21 Bloss, E. B. *et al.* Structured Dendritic Inhibition Supports Branch-Selective Integration in CA1 Pyramidal Cells. *Neuron* **89**, 1016-1030, doi:10.1016/j.neuron.2016.01.029 (2016).

22 Taniguchi, H. *et al.* A resource of Cre driver lines for genetic targeting of GABAergic neurons in cerebral cortex. *Neuron* **71**, 995-1013, doi:10.1016/j.neuron.2011.07.026 (2011).

23 Leao, R. N. *et al.* OLM interneurons differentially modulate CA3 and entorhinal inputs to hippocampal CA1 neurons. *Nat Neurosci* **15**, 1524-1530, doi:10.1038/nn.3235 (2012).

24 Han, X. *et al.* A high-light sensitivity optical neural silencer: development and application to optogenetic control of non-human primate cortex. *Front Syst Neurosci* **5**, 18, doi:10.3389/fnsys.2011.00018 (2011).

25 Vaidya, S. P., Li, G., Chitwood, R. A., Li, Y. & Magee, J. C. Formation of an expanding memory representation in the hippocampus. *Nat Neurosci* **28**, 1510-1518, doi:10.1038/s41593-025-01986-3 (2025).

26 Priestley, J. B., Bowler, J. C., Rolotti, S. V., Fusi, S. & Losonczy, A. Signatures of rapid plasticity in hippocampal CA1 representations during novel experiences. *Neuron* **110**, 1978-1992 e1976, doi:10.1016/j.neuron.2022.03.026 (2022).
27 Lin, J. Y., Knutsen, P. M., Muller, A., Kleinfeld, D. & Tsien, R. Y. ReaChR: a red-shifted variant of channelrhodopsin enables deep transcranial optogenetic excitation. *Nat Neurosci* **16**, 1499-1508, doi:10.1038/nn.3502 (2013).
28 Lillicrap, T. P., Santoro, A., Marris, L., Akerman, C. J. & Hinton, G. Backpropagation and the brain. *Nat Rev Neurosci* **21**, 335-346, doi:10.1038/s41583-020-0277-3 (2020).
29 Bengio, Y. Deriving differential target propagation from iterating approximate inverses. *arXiv preprint arXiv:2007.15139* (2020).
30 Aceituno, P. V., de Haan, S., Loidl, R., Beumer, L. & Grewe, B. F. Challenging Backpropagation: Evidence for Target Learning in the Neocortex. *bioRxiv*, 2024.2004.2010.588837, doi:10.1101/2024.04.10.588837 (2025).
31 Dudok, B. *et al.* Retrograde endocannabinoid signaling at inhibitory synapses in vivo. *Science* **383**, 967-970, doi:10.1126/science.adk3863 (2024).
32 Grienberger, C., Milstein, A. D., Bittner, K. C., Romani, S. & Magee, J. C. Inhibitory suppression of heterogeneously tuned excitation enhances spatial coding in CA1 place cells. *Nat Neurosci* **20**, 417-426, doi:10.1038/nn.4486 (2017).
33 Valero, M. *et al.* Cooperative actions of interneuron families support the hippocampal spatial code. *Science* **389**, eadv5638, doi:10.1126/science.adv5638 (2025).
34 Lovett-Barron, M. *et al.* Dendritic inhibition in the hippocampus supports fear learning. *Science* **343**, 857-863, doi:10.1126/science.1247485 (2014).
35 Geiller, T. *et al.* Large-Scale 3D Two-Photon Imaging of Molecularly Identified CA1 Interneuron Dynamics in Behaving Mice. *Neuron* **108**, 968-983 e969, doi:10.1016/j.neuron.2020.09.013 (2020).
36 Rolotti, S. V. *et al.* Local feedback inhibition tightly controls rapid formation of hippocampal place fields. *Neuron* **110**, 783-794 e786, doi:10.1016/j.neuron.2021.12.003 (2022).
37 Sheffield, M. E. J., Adoff, M. D. & Dombeck, D. A. Increased Prevalence of Calcium Transients across the Dendritic Arbor during Place Field Formation. *Neuron* **96**, 490-504 e495, doi:10.1016/j.neuron.2017.09.029 (2017).
38 Milstein, A. D. *et al.* Inhibitory Gating of Input Comparison in the CA1 Microcircuit. *Neuron* **87**, 1274-1289, doi:10.1016/j.neuron.2015.08.025 (2015).
39 Lovett-Barron, M. *et al.* Regulation of neuronal input transformations by tunable dendritic inhibition. *Nat Neurosci* **15**, 423-430, S421-423, doi:10.1038/nn.3024 (2012).
40 Vaasjo, L. O. *et al.* Dendritic inhibition terminates plateau potentials in CA1 pyramidal neurons. *bioRxiv*, doi:10.1101/2025.06.05.657434 (2025).
41 Tamboli, S. *et al.* Mouse hippocampal CA1 VIP interneurons detect novelty in the environment and support recognition memory. *Cell Rep* **43**, 114115, doi:10.1016/j.celrep.2024.114115 (2024).
42 Neubrandt, M., Lenkey, N. & Vervaeke, K. VIP interneurons control hippocampal place cell remapping through transient disinhibition in novel environments. *bioRxiv*, 2025.2002.2001.636072, doi:10.1101/2025.02.01.636072 (2025).
43 Kaufman, A. M., Geiller, T. & Losonczy, A. A Role for the Locus Coeruleus in Hippocampal CA1 Place Cell Reorganization during Spatial Reward Learning. *Neuron* **105**, 1018-1026 e1014, doi:10.1016/j.neuron.2019.12.029 (2020).

44 Takeuchi, T. *et al.* Locus coeruleus and dopaminergic consolidation of everyday memory. *Nature* **537**, 357-362, doi:10.1038/nature19325 (2016).
45 Wang, M. *et al.* Alpha2A-adrenoceptors strengthen working memory networks by inhibiting cAMP-HCN channel signaling in prefrontal cortex. *Cell* **129**, 397-410, doi:10.1016/j.cell.2007.03.015 (2007).
46 Bell, L. A., Bell, K. A. & McQuiston, A. R. Activation of muscarinic receptors by Ach release in hippocampal CA1 depolarizes VIP but has varying effects on parvalbumin-expressing basket cells. *J Physiol* **593**, 197-215, doi:10.1113/jphysiol.2014.277814 (2015).

Online methods

All experiments were performed according to methods approved by the Institutional Animal Care and Use Committees at Baylor College of Medicine (Protocol AN-7734) and Brandeis University (Protocols 22022 & 25001).

Surgery

Experiments were conducted on either sex of adult (older than two months postnatal) SST-IRES-Cre[22] (n = 23, JAX, #018973, also kindly provided by Andreas Tolias), Chrna2α-Cre[23] (n=21, kindly provided by Simon Chamberland, Richard Tsien, Jun Wu, and Gina Poe), and GP5.17[47] (n=4, JAX, #025393) mice, as well as double transgenic Chrna2α-Cre:GP5.17 (n=14), and Chrna2α-Cre:ReaChR[27] (JAX, #024846) mice (n=16). Mice were housed in a reverse light cycle facility (12 hours dark/12 hours light) maintained at 30-50% humidity and 21 °C. Surgeries were performed using stereotactic methods while mice were kept under deep anesthesia using isoflurane. Following local antisepsis and the application of a topical anesthetic, the scalp was removed and the skull cleaned. Then, the skull was leveled, and two craniotomy locations for virus injections in dorsal CA1 were marked (2.15 mm | 2.35 mm posterior from bregma, 1.8 mm | 2.2 mm lateral from the midline) as well as the center location of a cranial window (2.2 mm posterior from bregma and 2.0 mm lateral from the midline). Following the virus injection, a 3 mm diameter craniotomy was made above the hippocampus, and the cortical tissue above the hippocampus was aspirated while rinsed with 0.9% sterile saline. Once the hippocampal capsule was visible, the window implant (a 3 mm-diameter, 1.7 mm-high metal cannula (McMaster) with a window on the bottom and 0.5 mm of shrink tubing around the top) was implanted and cemented in place. Lastly, a titanium head bar was secured to the skull using dental acrylic (Ortho-Jet, Lang Dental). Virus

429 injections were carried out using a microinjector (Drummond, Nanoject II) loaded with a pulled
430 glass pipette that was trimmed and beveled to 25-35 μm and backfilled with mineral oil (Sigma).
431 The virus was loaded by retracting the injector's plunger. The microinjector was positioned over
432 the craniotomies using a micro-manipulator (MP-285A, Sutter Instruments). For each injection
433 site, a 0.5 mm round craniotomy was drilled, and 46 nl of virus dilution was injected at two depths
434 per site (1200-1300 μm and 1000-1050 μm). Virus injections varied across experimental
435 paradigms. For imaging SST-OLM axons: AAV2/1.Syn.Flex.GCaMP6f.WPRE.SV40 (Addgene,
436 #100833-AAV1, titer: 8×10^{11}-2×10^{12}) with AAV2/1-syn-Flex-TdTomato (UNC Neurotools, titer:
437 3-9×10^{10}). For imaging Chrna2α-OLM somata: AAV2/1.Syn.Flex.GCaMP6f.WPRE.SV40
438 (titer:8×10^{11}-2×10^{12}). For inhibition of Chrna2α-OLMs: AAV2/1.hsyn.Flex.ArchT.tdTomato
439 (UNC Neurotools, titer: 3.3×10^{11}), or AAV2/1.hsyn.Flex.ArchT.tdtomato (UNC Neurotools, titer:
440 3.3×10^{11}) with AAV2/1.Syn.GCaMP6f.WPRE.SV40 (Addgene, #100837, titer: 1-3×10^{12}). For
441 inhibition controls: AAV2/1-syn-Flex-tdTomato (UNC Neurotools, titer: 3×10^{9}-9×10^{10}), or
442 AAV2/1-syn-Flex-tdTomato (UNC Neurotools, titer: 3×10^{9}-9×10^{10}) with
443 AAV2/1.Syn.GCaMP6f.WPRE.SV40 (Addgene: #100837-AAV1, titer: 1-3×10^{12}). For activation
444 of Chrna2α-OLMs and controls: AAV2/1.Syn.GCaMP6f.WPRE.SV40 (Janelia Viral Core,
445 titer:1×10^{12}).
446
447 *Behavioral training and task on the linear track treadmill*
448 The treadmill comprised a fabric belt (180 cm; McMaster Carr) and a custom-built lick port that
449 dispensed sucrose water, controlled by a solenoid valve (quiet operation; The Lee Company). The
450 belt was self-propelled by the animal, and its speed was tracked using an encoder at the front wheel
451 axle. An Arduino-based behavioral state machine and corresponding MATLAB GUI (Bpod,
452 Sanworks) were used to control the reward value and sensors, and to track the encoder. A custom-
453 written MATLAB GUI controlled the light for optogenetic manipulations. The behavioral data,
454 stimulations, and frame times were monitored and recorded using a NIDAQ-based acquisition
455 system (National Instruments, PCIe-6341) and the MATLAB-based Wavesurfer software (version
456 0.982, Janelia).

457 5 to 7 days following surgery, the mice were placed on a water restriction protocol
458 (receiving 1.5ml per day). Three or four days into water restriction, animals were habituated to the

459 experimenter for 5-6 days, followed by 3-5 days of head-fixed treadmill training. Training days
460 were conducted during the animal's dark cycle on a belt with no cues and with a sucrose reward
461 (5-10% solution) dispensed at a random location each lap. During experimental days, the mice
462 learned to navigate a cue-rich belt (three cue sections: Velcro tape patches, thin hot glue sticks,
463 and correction fluid dots) to a single fixed location for a sucrose reward. In the light-cue learning
464 experiments (Extended Data Fig. 2), the animals were on a blank belt (no tactile cues) and received
465 a bilateral visual stimulus of blue light (10 Hz for 500 ms) 50 cm before the fixed reward location.
466 For OLM activity experiments, recordings lasted 30-60 minutes. Mice were excluded if they ran
467 <75 laps or >350 laps in 60 minutes. Mice recorded past day 1 (Extended Data Fig. 1) were
468 recorded for a maximum of five more days. For the optogenetic experiments, analyses were limited
469 to 88-120 laps (mean±SEM: 101±1 laps) per session. Animals were recorded at most once per day.

470

471 *In vivo two-photon Ca^{2+} imaging*

472 All experiments were conducted in a dark box, and Ca^{2+} images were captured using custom-built
473 two-photon microscopes (detailed descriptions below). Experiments recording OLM interneuron
474 activity were performed on both microscopes. Optogenetic experiments activating ArchT or
475 ReachR were performed on the microscopes at Brandeis or Baylor, respectively. The images were
476 recorded using ScanImage at 30 Hz and 512 x 512 pixels. Fields of view were 280 x 280 um and
477 for animals with multiple recording days, we attempted to return to the same field of view
478 (Extended Data Fig. 1a). GCaMP6f, and in some cases tdTomato or Citrine, were imaged through
479 Nikon 16x, 0.8-numerical-aperture objectives (both microscopes) and excited at 920 nm (typically
480 30-75 mW measured under the objective)

481 For experiments conducted at Baylor recording the activity of CA1 OLM interneurons, the
482 microscope (Janelia MIMMS 2.0 design) used a Ti:Sapphire laser (Coherent, Chameleon Ultra II),
483 passed through a FF705-Di01 (Semrock) primary dichroic filter. Images were collected with
484 ScanImage R2022 premium software (Vidrio). Emission light passed through a 565 DCXR
485 dichroic filter (Chroma) and either stacked 505/19 nm (GCaMP6f channel; Semrock) and 514/44
486 nm (GCaMP6f channel; Semrock), or a 612/69 nm (tdTomato channel, Semrock) bandpass filters.
487 Light was detected by two GaAsP photomultiplier tubes (11706P-40SEL, Hamamatsu). For
488 optogenetic ReaChR manipulation experiments, in which only the GCaMP6f channel was

489 recorded, a 594 nm laser (Obis, Coherent) was used. Diffuse 594 nm light was reflected into the
490 beam path by a DMLP805R (Semrock) dichroic filter, and the primary dichroic was substituted
491 with a Di02-R561 (Semrock) dichroic filter.

492 For experiments conducted at Brandeis, the microscope at Brandeis (INSS, UK) included
493 a Spectra-Physics Insight X3 laser. Images were collected with ScanImage R2021 software
494 (Vidrio). Emission light passed through a T565lpxr (Chroma) dichroic filter and either an ET
495 510/80 nm (GCaMP6f channel, Chroma) or a 630/75 nm (tdTomato channel, Chroma) bandpass
496 filter, then was detected by respective GaAsP photomultiplier tubes (11706P-40, Hamamatsu). For
497 optogenetic ArchT manipulation experiments, in which only the GCaMP6f channel was recorded,
498 diffuse 594 nm light from an LED (Thorlabs) passed through an ET570LP (Chroma) low-pass
499 filter, and the filter in front of the PMT in the GCaMP6f channel was replaced with an ET 510/80
500 (Chroma) bandpass filter stacked between two BG39 (Chroma) filters.

501

502 *Optogenetic perturbation of CA1 OLM interneurons*

503 To examine the effect of OLM inhibition (performed on the microscope at Brandeis), we used the
504 following groups: 1) experimental mice (Chrna2α-Cre:GP5.17 injected with
505 AAV2/1.hsyn.Flex.ArchT.tdtomato, n=6; Chrna2α-Cre injected with
506 AAV2/1.hsyn.Flex.ArchT.tdtomato and AAV2/1.Syn.GCaMP6f.WPRE.SV40, n=3); 2) control
507 mice (Chrna2α-Cre:GP5.17 injected with AAV2/1.hsyn.Flex.tdtomato, n=8; Chrna2α-Cre
508 injected with AAV2/1.hsyn.Flex.tdtomato and AAV2/1.Syn.GCaMP6f.WPRE.SV40, n=2; non-
509 injected GP5.17, n=4). The experimental (ArchT-expressing) and control mice underwent the
510 same procedures and paradigm: the window was implanted in the same surgery as the injections.
511 Imaging and optogenetic experiments were conducted 18 to 28 days post-surgery. Recordings were
512 obtained on days 1–3 under the otherwise same conditions. Continuous diffuse light of 594 nm
513 from an LED (Thorlabs) at 4 mW measured under the objective was delivered through the
514 objective. In all optogenetic experiments, the region of the belt where 594 nm light was applied
515 (the "opto-zone") was 60 cm centered at the reward location. Light was applied only in block 2
516 (approximately 50 laps) when the animals were around the fixed reward location (10 – 70 cm);
517 there was no time limit. To validate the effect of ArchT on OLM activity (Extended Data Fig. 3a-
518 f), a subset of Chrna2α-Cre mice that expressed both GCaMP6f and ArchT (n=3) or tdT (n=2)

519 were used. A field of view was located that contained OLM neurons expressing GCAMP6f, and
520 these neurons were or were not expressing ArchT or tdTomato, respectively. The Ca^{2+} signals of
521 these cells were recorded while the LED was on for approximately 2.5-3 seconds, or, in some laps,
522 for 60 cm of the animal's travel on the belt.

523 To examine the effect of OLM excitation (performed on the microscope at Baylor), we
524 used the following groups: 1) experimental mice (Chrna2α-Cre:ReaChR injected with
525 AAV2/1.Syn.GCaMP6f.WPRE.SV40, n=8); 2) littermate control mice (Chrna2a-Cre:ReaChR
526 litter mates that were confirmed by genotype to lack at least one allele required for ReaChR
527 expression, injected with AAV2/1.SynGCaMP6f.WPRE.SV40, n=8). The experimental ReaChR-
528 expressing mice and littermate control mice underwent the same procedures and paradigm as
529 ArchT mice in OLM inhibition experiments. Optogenetic manipulation in ReaChR-expression
530 animals was restricted to day 1 on the cue-enriched, fixed-reward belt. Diffuse light of 594 nm
531 was delivered from a laser (Obis, Coherent) at 40 Hz (square pattern) at 0.8-0.95 mW measured
532 under the objective. 594 nm light was only applied during block 1 (50 laps) while the mouse was
533 within the opto-zone. The laser was turned off if the mouse's velocity dropped below 2.5 cm/s, or
534 if it had been applied for more than 5s continuously. To validate the effect of ReaChR activation
535 on OLM activity in mice used for the data presented in Fig. 4, stratum oriens interneurons were
536 found directly above the field of view used for pyramidal neuron recordings, on the last day of
537 experimentation (Extended Data Fig. 3g-l). The Ca^{2+} signals of these interneurons were recorded
538 while the laser was either activated for 5 seconds ("fixed-duration", n=8 mice) or within the opto-
539 zone ("fixed-location", n=7 mice). Each mouse was validated to have responsive OLMs, which
540 showed> 2-fold increases in mean Δf/f while the laser was on (for fixed-duration: a 3s window
541 before stimulation was compared with a 4s window during; for fixed-location: the opto-zone was
542 compared with surrounding locations).

543

544 *Data analysis*

545 *Ca^{2+} signal extraction and activity map generation*

546 To extract axonal Ca^{2+} signals from the population of CA1 SST-expressing OLM interneurons,
547 motion correction was performed using the Suite2p pipeline[48], with both green (GCaMP6f) and
548 red (tdTomato) channels aligned, and the red channel used for image registration. GCaMP6f
549 fluorescence was then averaged across the field of view using custom MATLAB functions (version

2024b), excluding a narrow border (2% of frame width) to minimize motion-related artifacts. For somatic Ca^{2+} imaging, motion correction and ROI detection were performed using Suite2p on GCaMP6f fluorescence. Functional ROIs were detected for Chrna2α-expressing OLM somata. For pyramidal neurons in ArchT mice, ROIs were identified using a custom-pretrained Cellpose[49] model. In ReaChR mice, which exhibited dense pyramidal neuron labeling, functional ROI detection was used and cross-validated with the same Cellpose model. All ROIs were manually curated, and those with insufficient signal quality were excluded. In recordings from the stratum pyramidale in ReaChR mice, interneurons were identified based on event amplitude, duration, and frequency, and manually removed. All datasets in which motion correction was unsuccessful were excluded.

Further analyses were performed using custom MATLAB code. First, raw fluorescence signals were converted to Δf/f, calculated as $(f - f_0)/f_0$. For pyramidal neurons, f_0 was defined as the mode of the fluorescence histogram, whereas for OLM interneurons, f_0 was defined as the 8th percentile of fluorescence values. For pyramidal cell recordings, this was followed by neuropil correction (subtraction of 70% of the neuropil Δf/f signal obtained via Suite2p) and the generation of spatial activity maps by dividåing the 180-cm belt (one lap) into 50 spatial bins (3.6 cm each). For each lap, mean Δf/f values were computed within each spatial bin during periods when running speed exceeded 2.5 cm/s. These spatially binned activity maps were used to calculate noise correlations between neighboring ROIs (within three soma diameters). Pearson's correlation coefficient thresholds of 0.35–0.5 were applied to identify potential signal cross-contamination, and contaminated ROIs were excluded from further analysis. For interneuron recordings, spatial Δf/f maps were multiplied by the animal's dwell time within each spatial bin to account for learning-related changes in running speed and isolate spatial patterns of inhibitory activity. Dwell time was computed as d_{bin}/V_{bin}, where d_{bin} is the spatial bin width (3.6 cm), and V_{bin} is the mean velocity within that bin. Significant Ca^{2+} events were identified as transients exceeding three standard deviations of the baseline noise (mode of the histogram). For visualization, spatial maps were smoothed using a three-point boxcar filter and centered such that either the reward location (cue-belt environment) or the visual cue location (visual cue environment) corresponded to spatial bin 25.

581 *CA1 place cell identification*

582 Place cells were determined as previously described[3,18]. In brief, from each CA1 pyramidal
583 neuron's spatial map of mean Δf/f, we first identified potential onset laps for a place field
584 (induction lap). Place fields were defined as those spatial bins with contiguous activity >20% of
585 the peak mean Δf/f. Induction occurred at a lap where significant Ca^{2+} activity was within the
586 neuron's eventual place field, and two out of the following five laps also had significant activity
587 in the eventual place field. If multiple laps fit these criteria per neuron, the first instance was the
588 induction unless the place field generated was weak and disappeared for more than 20 laps at some
589 point. Only the laps following place field induction were used to determine place cell identity.
590 CA1 place cells were defined as neurons exhibiting (1) significant spatial information about the
591 linear track position (outside the 95% confidence interval of values obtained from shuffled data)
592 and (2) high place field reliability, defined as significant activity on more than 33% of laps
593 following place field induction. The spatial information was calculated as described previously[18]
594 and compared to 100 shuffles of the activity. For shuffling, Δf/f from periods when the mouse's
595 velocity exceeded 2.5 cm/s was circularly rotated 500 frames and divided evenly into six sections
596 that were permuted in pseudo-random order. Place cells were determined independently across the
597 laps of blocks 1 and 2, within which only one place field was used per neuron. If the spatial bin
598 containing the peak of a place cell's place field moved by >20 cm between the laps of blocks 1
599 and 2, its block 2 place field was considered a new place field for that cell.

600

601 *Plateau detection*

602 Only cells with at least 20 significant events (amplitude > three times the standard deviation of
603 baseline noise) were included in this analysis. Putative plateau (Figure 3-4) events were identified
604 using criteria adapted from previous whole-cell recordings and descriptions of GCaMP6f imaging
605 of Ca^{2+} events[1,3,25,26]. Putative plateaus were defined as events that (1) were large Ca^{2+} transients,
606 reaching amplitudes within the top 10% of all significant events for each neuron, and > 1Δf/f; (2)
607 were followed by significant activity within 45 cm of the event peak in at least three of the
608 subsequent five laps; (3) were followed by a forward shift (relative to the event peak) in the mean
609 Δf/f center of mass across the subsequent five laps; (4) Only one event per cell, i.e., the first event
610 meeting criteria (1)-(3), was included in subsequent analyses (the exception is Extended Data Fig.
611 5 a, b, d, e; see below). Plateau identification was performed across all cells, regardless of spatial

location. Spatial maps of plateaus were generated for each cell, wherein every spatial bin x lap was scored as having a plateau (1) or not (0). Plateau probability per animal for blocks 1 and 2 was calculated as the total number of detected plateau events within each spatial bin (10 bins, 18 cm per bin), normalized by the number of regions of interest (ROIs) in the animal. For Extended Data Fig. 5a, b, d, e, only plateau events from place cells that occurred within their place field at or following the place field induction were included. For correlation between velocity and place field width, the mean velocity (cm/s) across the time points of every $\Delta f/f$ value averaged within the spatial bin containing the peak of the plateau event was used versus the place field computed over the ten following laps.

Behavioral data quantification

As with the analysis of Ca^{2+} data, spatial maps for behavioral data were constructed by first dividing the belt length (also one lap, 180 cm) into 50 spatial bins (3.6 cm each). Along all laps, the mean velocity was averaged within each spatial bin. Lick probability was computed by scoring each spatial bin as containing (1) or lacking (0) at least one lick by the mouse, then by taking the mean along this binary matrix.

Statistical methods.

The exact sample size (n) for each experimental group is indicated in the figure legend or in the main text. No statistical methods were used to predetermine sample sizes, but our sample sizes are similar to those reported in previous publications. In some cases, when the data distribution was assumed but not formally tested to be normal, data were analyzed using two-tailed paired or unpaired *t*-tests, as stated in the text or figure legends. Data were analyzed automatically without consideration of trial conditions or experimental groups. Experiments and data analyses were not randomized and not performed blind to the experimental conditions. If not otherwise indicated in the figure, data are shown as mean ± SEM.

Data Availability

The data that support the findings of this study are available from the corresponding author upon request.

643 *Code Availability*

644 The code that supports the findings of this study is available from the corresponding author upon
645 request.

646

647 47 Dana, H. *et al.* Thy1-GCaMP6 transgenic mice for neuronal population imaging in vivo.
648 *PLoS One* **9**, e108697, doi:10.1371/journal.pone.0108697 (2014).
649 48 Pachitariu, M. *et al.* Suite2p: beyond 10,000 neurons with standard two-photon
650 microscopy. *BioRxiv* (2017).
651 49 Stringer, C. & Pachitariu, M. Cellpose3: one-click image restoration for improved cellular
652 segmentation. *Nat Methods* **22**, 592-599, doi:10.1038/s41592-025-02595-5 (2025).

653

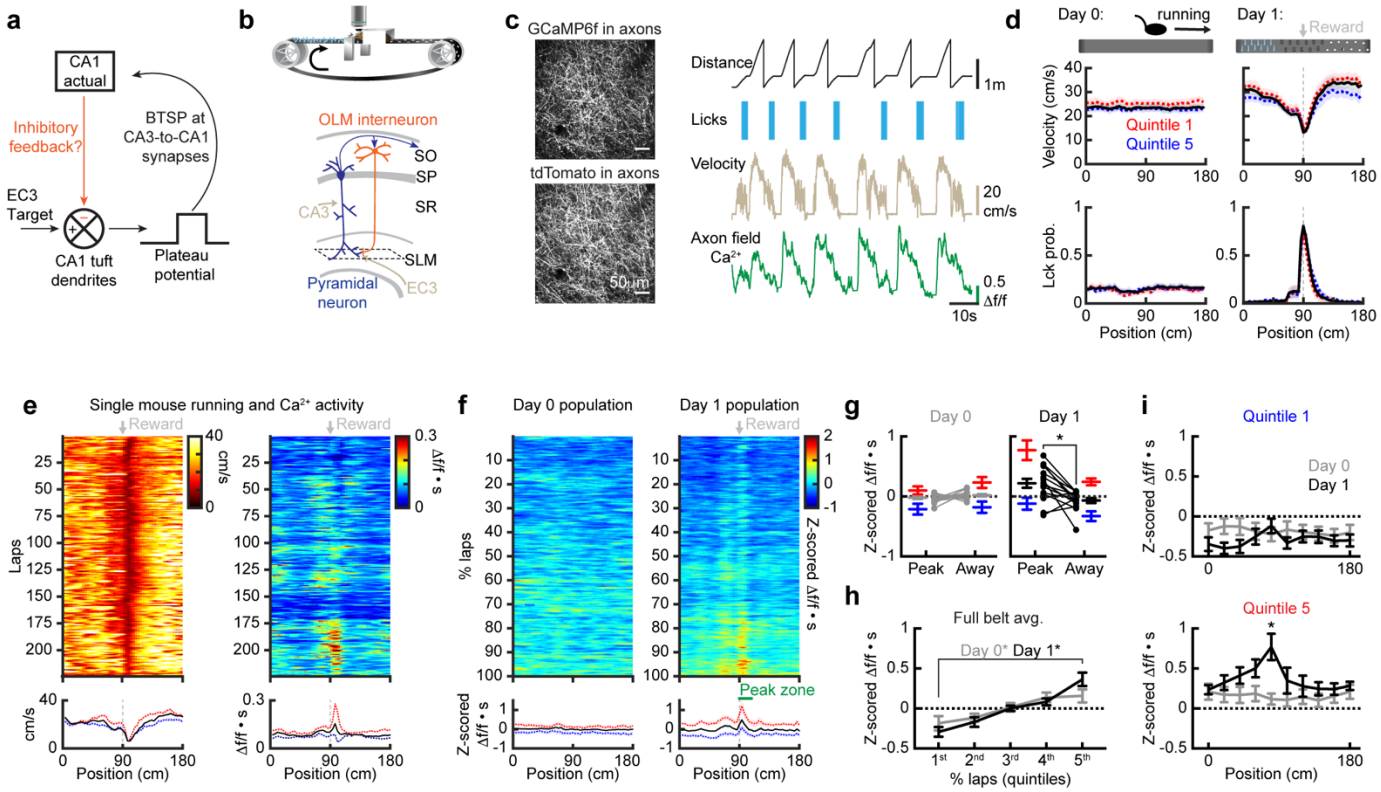

Figure 1: OLM population activity during learning.

a, Preliminary BTSP working model. **b**, Top: experimental setup, in which mice learn the location of a water reward. Bottom: schematic of the CA1 microcircuit and imaging plane (dashed line) **c**, Left: representative, two-photon, time-averaged images of axons from CA1 SST-OLMs expressing GCaMP6f and tdTomato. Right: example traces of distance, licking, velocity, and GCaMP6f Δf/f (mean of the field). **d**, Top: Task design of day 0 (the last day of habituation), and day 1 (the first day of learning). Middle: mean running profile across space. Bottom: mean lick probability across space. **e**, Representative day 1 running, and Δf/f corrected for dwell time (•s). Top: along laps. Bottom: spatial profiles. **f**, Days 0 and 1 mean z-scored Δf/f•s (day 0: n=15, day 1: n=15). Top: along the percentage of laps run. Bottom: spatial profiles. The peak-zone is 90 cm beginning at the spatial bin with reward, the away-zone is the same but 90 cm away. **g**, Days 0 and 1 mean z-scored Δf/f•s within peak-zone and away-zone (paired two-tailed *t*-test, day 1: $P=2.8\cdot10^{-3}$). **h**, Mean z-scored Δf/f•s vs. lap quintiles (two-way RM ANOVA with post-hoc FDR correction, group x quintile: $P=9.7\cdot10^{-3}$, day 0: $P=1.9\cdot10^{-2}$, day 1: $P<1\cdot10^{-4}$). **i**, Quintiles 1 and 5 mean z-scored Δf/f•s vs. position (bin=18 cm, two-way RM ANOVA with post-hoc FDR correction, quintile 1/group x bin: $P=7.0\cdot10^{-4}$, quintile 5/group x bin: $P<1\cdot10^{-4}$, quintile 5/bin 5: $P<1\cdot10^{-4}$). In **d-i,** n=15 mice. In **g,** dots represent mice. Data are shown as mean ± s.e.m.

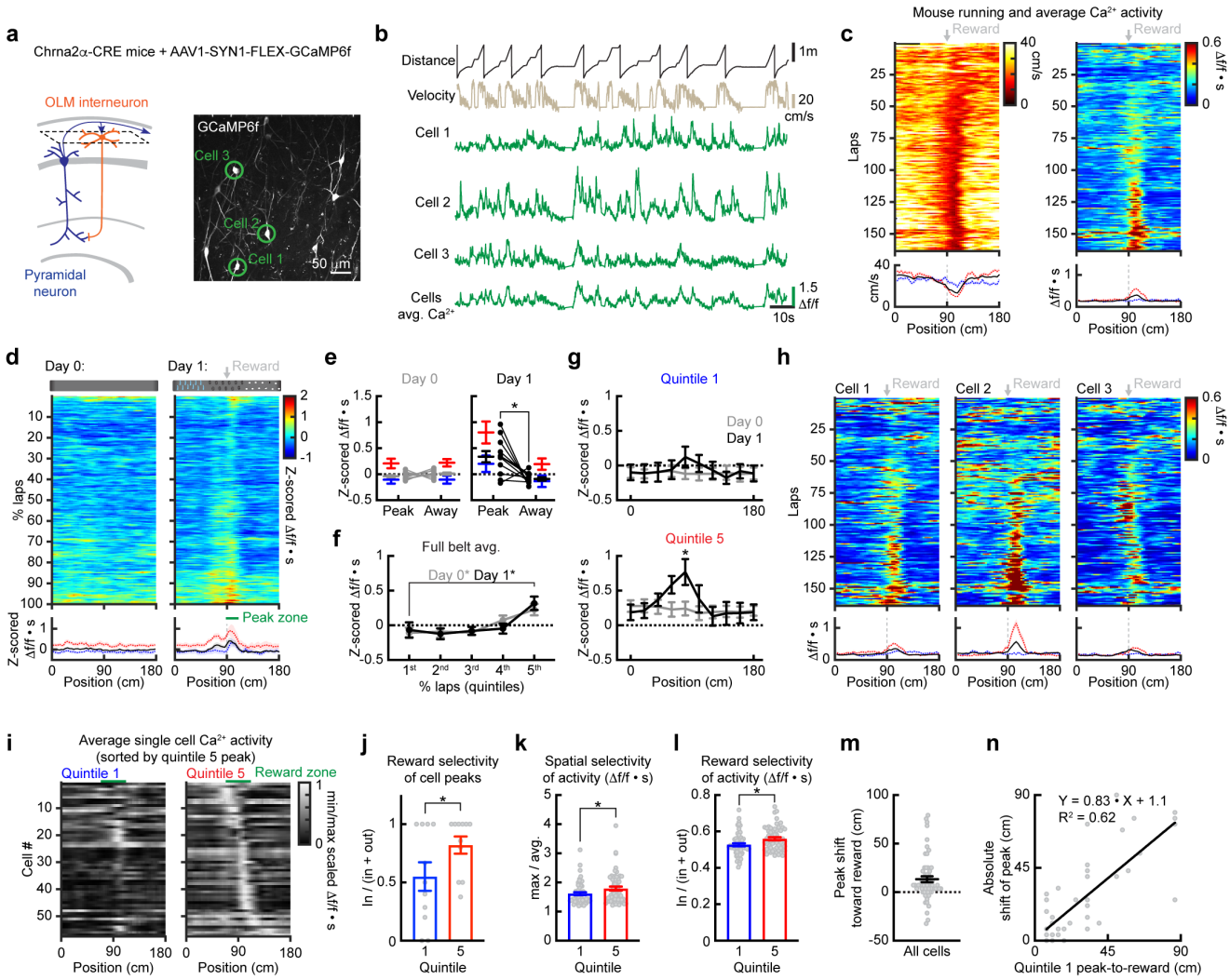

Figure 2: Single-cell OLM activity during learning.

a, Left: Schematic of the CA1 microcircuit with imaging plane (dashed line). Right: representative, two-photon, time-averaged image of Chrna2α-OLMs expressing GCaMP6f. **b**, Example traces of distance, velocity, and Δf/f for three OLM neurons and the mean of all neurons in the field. **c**, Representative day 1 running and mean Δf/f•s. Top: along laps. Bottom: spatial profiles. **d**, Top: Task design of day 0 and day 1. Middle: mean z-scored Δf/f•s along the percentage of laps run. Bottom: spatial profiles. The peak-zone is 90 cm beginning at the spatial bin with reward, the away-zone is the same but 90 cm away. **e**, Days 0 and 1 mean z-score Δf/f•s within the peak-zone and away-zone (paired two-tailed *t*-test, day 1: $P=8.8\cdot10^{-3}$). **f**, Mean z-scored Δf/f•s vs. lap quintiles (Two-way RM ANOVA with post-hoc FDR correction, day 0: $P=3.4\cdot10^{-2}$, day 1: $P=1.1\cdot10^{-2}$). **g**, Quintiles 1 and 5 mean z-score Δf/f•s vs. position (Two-way RM ANOVA with post-hoc FDR correction, quintile 5/group x bin: $P=7\cdot10^{-4}$, quintile 5/bin 5: $P=1.8\cdot10^{-3}$). **h**, Representative day 1 Δf/f•s for three OLM neurons. Top: along laps. Bottom: spatial profiles. **i**, Min/max scaled mean Δf/f•s for all neurons (n=55 neurons, scaling from quintiles 1 and 5, sorted by quintile 5 peak). The reward zone is 39.6 cm centered at the reward. **j**, Mouse reward selectivity (the fraction of neurons with mean Δf/f•s peaks within the reward-zone (paired two-tailed *t*-test, $P=2.0\cdot10^{2}$). **k**, OLM Spatial selectivity (max/mean Δf/f•s, paired two-tailed *t*-test, $P=4.4\cdot10^{-2}$). **l**, OLM reward selectivity (the fraction of mean Δf/f•s within the reward-zone, paired two-tailed *t*-test, $P=1.1\cdot10^{-2}$). "In" and "out" refer to activity inside or outside the reward zone. **m**, Mean distance that Δf/f•s peaks shifted toward reward from quintile 1 to 5. **n**, The absolute distance Δf/f•s peaks shifted from quintile 1 to 5, vs. the absolute peak-to-reward distance in quintile 1. In **d-n** day 0: n=12 mice, day 1: n=11 mice. In **e,j** dots represent mice, and in **k-n** they represent neurons. Data are shown as mean ± s.e.m.

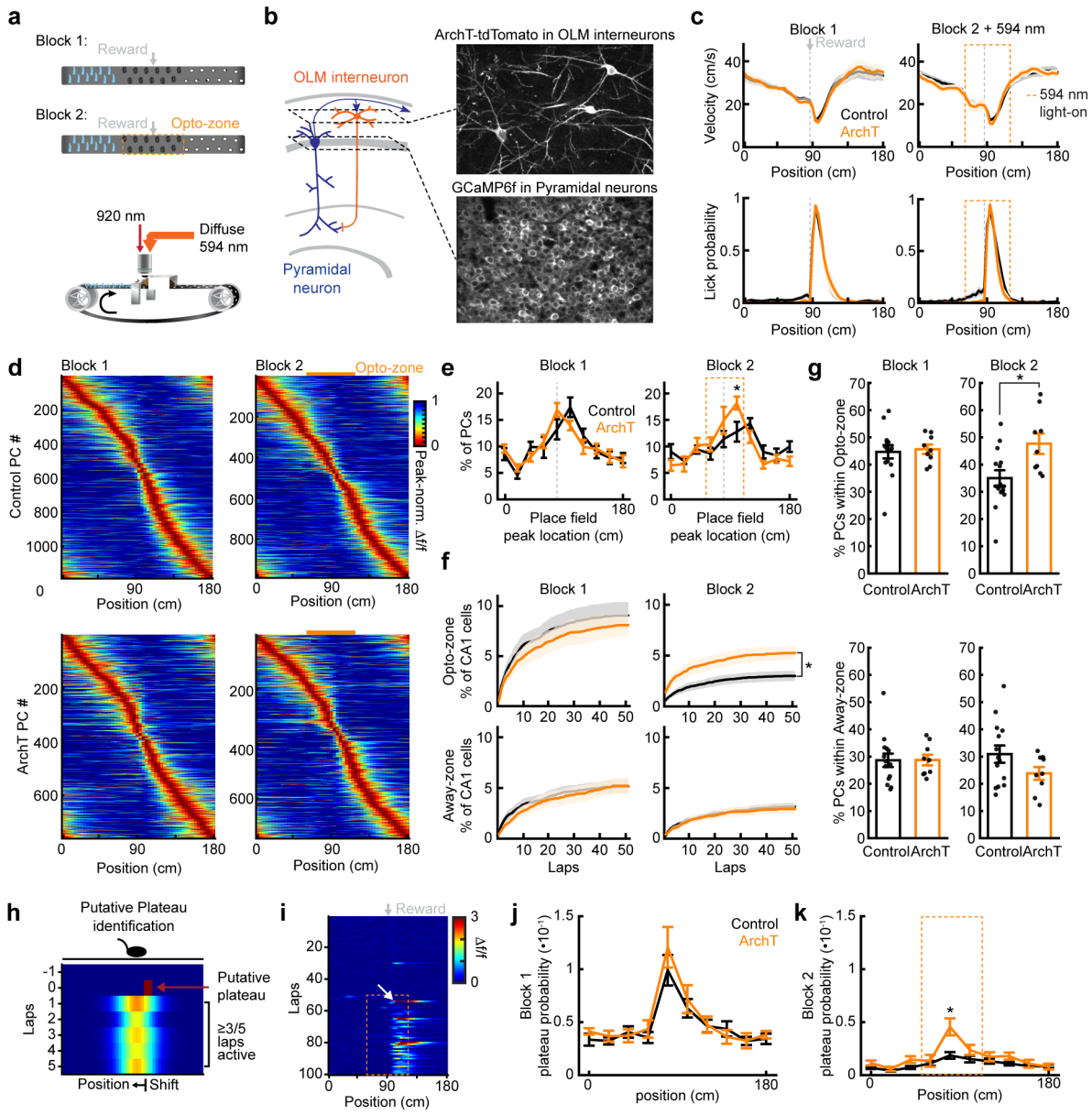

Figure 3: Silencing Chrna2α-OLMs late in learning.

a, Top: day 1 manipulation paradigm wherein ArchT in Chrna2α-OLMs is activated during block 2 (50-lap blocks) within 30 cm of the reward (the opto-zone is 60 cm, centered at the reward, the away-zone is the same, but 90 cm away from the opto-zone). Bottom: Imaging and optogenetics apparatus. **b**, Left: Schematic of the CA1 microcircuit with two imaging planes (dashed lines). Right: representative, two-photon, time-averaged images of Chrna2α-OLMs expressing Arch-tdTomato and pyramidal neurons expressing GCaMP6f. **c**, Blocks 1 and 2 behavior. Top: mean running profile across space. Bottom: mean lick probability across space. **d**, Blocks 1 and 2 peak-normalized mean Δf/f vs. position for all place cells. Analyzed independently within blocks, sorted by place field peak location. Top: control (block 1: n=1188, block 2: n=989). Bottom: ArchT (block 1: n=762, block 2: n=748). **e**, Blocks 1 and 2 fraction of CA1 place cells vs. place field peak location (unpaired two-tailed *t*-test: block 2/bin 5 $P=4\bullet10^{-2}$). **f,** Blocks 1 and 2 CA1 place cell onsets. Top: place cells with place field peaks within the opto-zone (two-tailed *t*-test, block 2: $P=1\bullet10^{-2}$). Bottom: same for away-zone. **g**, Place cell distributions in the opto-zone and away-zones. Left: block 1, Right: block 2 (unpaired two-tailed *t*-test, opto-zone: $P=1\bullet10^{-2}$). **h**, Schematic of criteria for putative plateaus. **i**, Example place cell from an ArchT mouse. Mean Δf/f along laps with putative plateau marked by the white arrow. **j-k**. Blocks 1 (**j**) and 2 (**k**) mean plateau probability for all cells vs. position (two-way RM ANOVA with post-hoc FDR correction, block 2/group x bin: $P=7\bullet10^{-4}$, block 2/bin 5: P=0.012). In **c-k**, control: n=14 mice, ArchT=9 mice. In **g** dots indicate mice. Data are shown as mean ± s.e.m.

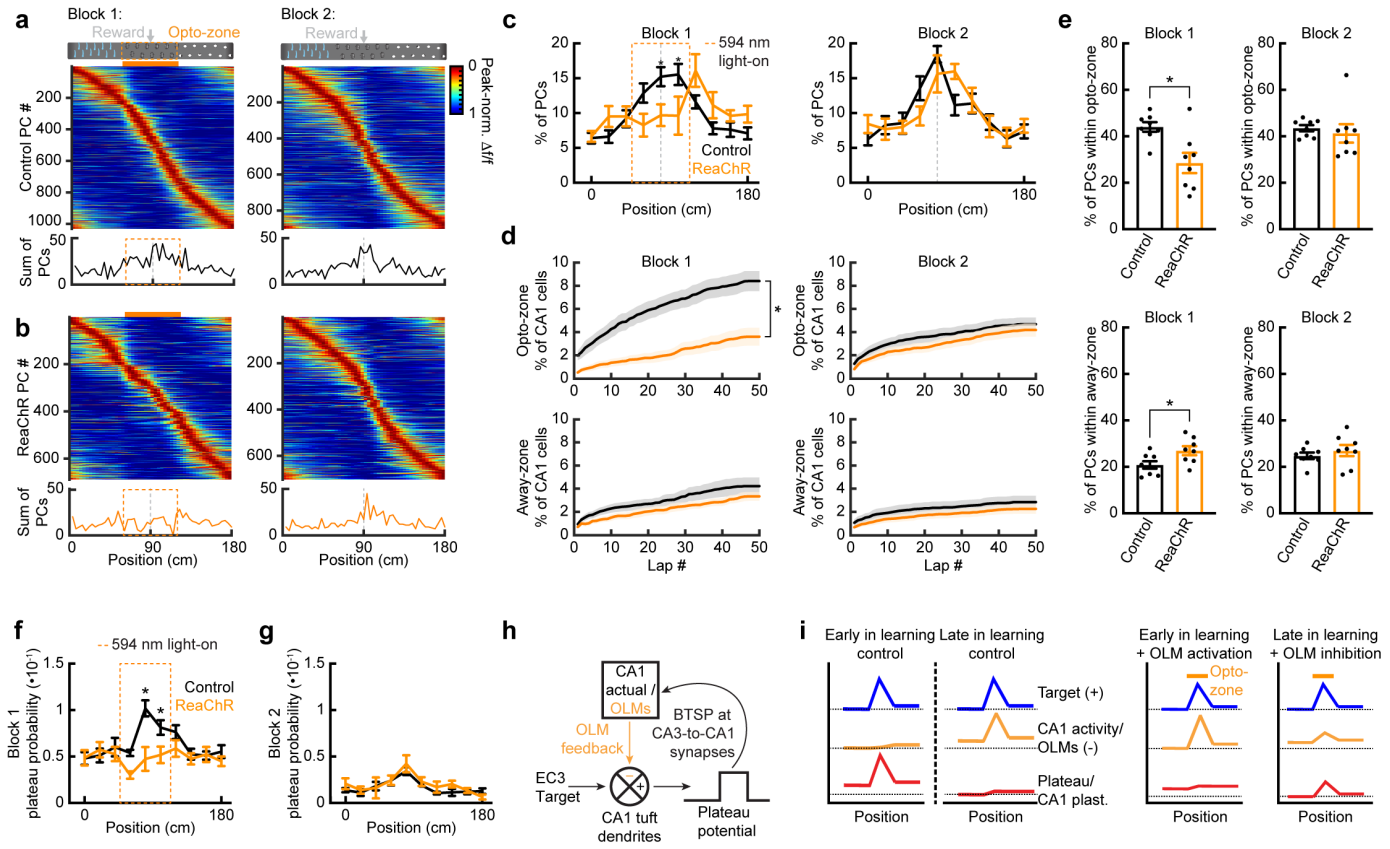

Figure 4: Activating Chrna2α-OLMs early in learning.

a, Top: manipulation paradigm wherein ReaChR in Chrna2α-OLMs is activated during block 1 (the opto-zone is 60 cm centered at the reward, the away-zone is the same, but 90 cm away from the opto-zone). Middle: Blocks 1 and 2 peak-normalized mean Δf/f vs. position for all place cells from control mice. Bottom: histogram showing place cell distribution (block 1: n=1031 cells, block 2: n=901 cells). Place cells were analyzed independently within blocks, sorted by place field peak location in the heatmaps. **b**, same as **a** for ReaChR mice (block 1: n=688 cells, block 2: n=702 cells). **c**, Blocks 1 and 2 fraction of CA1 place cells vs. place field peak location (bin=18 cm, two-way RM ANOVA with post-hoc FDR correction, block 1/group x bin: $P=1.0\cdot10^{-3}$, block 1/bin 5: $P=7.1\cdot10^{-3}$, block 1/bin 6: $P=4.0\cdot10^{-3}$). **d,** Blocks 1 and 2 CA1 place cell onsets. Top: place cells with place field peaks within the opto-zone (unpaired two-tailed *t*-test, block 1: $P=1.0\cdot10^{-3}$). Bottom: same as top for away zone. **e**, Place cell distributions in the opto-zone and away-zone. Left: block 1, (unpaired two-tailed *t*-test, opto-zone: $P=6.1\cdot10^{-3}$, away-zone: $P=2.8\cdot10^{-2}$). Right: block 2. **f-g**. Blocks 1 (**f**) and 2 (**g**) mean plateau probability for all cells vs. position (block 1 two-way RM ANOVA, block 1/group x quintile: $P=2.7\cdot10^{-3}$, block1/bin 5: $P<1\cdot10^{-4}$, block 1/bin 6: $P=7.2\cdot10^{-3}$). **h**, BTSP working model with OLM feedback added. **i**, Spatial profiles of the proposed signals in early and late learning that regulate BTSP and CA1 spatial representation. Left: typical learning in control animals. Right: manipulation of typical learning by either activation or inhibition of OLMs. In **a-g**, control: n=8 mice, ReaChR=8 mice. In **e**, the dots indicate mice. Data are shown as mean ± s.e.m.